# RESISTIVE EMERGENCE OF UNDULATORY FLUX TUBES

E. PARIAT, G. AULANIER, AND B. SCHMIEDER[1]

Laboratoire d'Etudes Spatiales et d'Instrumentation en Astrophysique (LESIA), Observatoire de Meudon, 5 place Jules Janssen,
F-92195 Meudon Cedex, France; etienne.pariat@obspm.fr

AND

M. K. GEORGOULIS, D. M. RUST, AND P. N. BERNASCONI

Applied Physics Laboratory, Johns Hopkins University, 11100 Johns Hopkins Road, Laurel, MD 20723-6099

*Received 2004 May 11; accepted 2004 June 23*

## ABSTRACT

During its 2000 January flight, the Flare Genesis Experiment observed the gradual emergence of a bipolar active region, by recording a series of high-resolution photospheric vector magnetograms and images in the blue wing of the Hα line. Previous analyses of these data revealed the occurrence of many small-scale, transient Hα brightenings identified as Ellerman bombs (EBs). They occur during the flux emergence, and many of them are located near moving magnetic dipoles in which the vector magnetic field is nearly tangential to the photosphere. A linear force-free field extrapolation of one of the magnetograms was performed to study the magnetic topology of small-scale EBs and their possible role in the flux emergence process. We found that 23 out of 47 EBs are cospatial with bald patches (BPs), while 15 are located at the footpoints of very flat separatrix field lines passing through distant BPs. We conclude that EBs can be due to magnetic reconnection, not only at BP locations, but also along their separatrices, occurring in the low chromosphere. The topological analysis reveals, for the first time, that many EBs and BPs are linked by a hierarchy of elongated flux tubes showing aperiodic spatial undulations, whose wavelengths are typically above the threshold of the Parker instability. These findings suggest that arch filament systems and coronal loops do not result from the smooth emergence of large-scale Ω-loops from below the photosphere, but rather from the rise of undulatory flux tubes whose upper parts emerge because of the Parker instability and whose dipped lower parts emerge because of magnetic reconnection. EBs are then the signature of this resistive emergence of undulatory flux tubes.

*Subject headings:* MHD — Sun: magnetic fields — Sun: photosphere

## 1. INTRODUCTION

The standard model for the formation of classical bipolar active regions relies on the gradual emergence through the photosphere of a more or less homogeneous large-scale subphotospheric flux tube, whose curvature always points downward during the emergence process. During the emergence, the upper parts of the flux tube are believed to form growing chromospheric arch filament systems (AFSs), as observed in Hα (e.g., Malherbe et al. 1998), which later result in a system of large Ω-loops, as observed in UV when they expand into the corona (Magara & Longcope 2001; Fan 2001). In this frame, the two intersections of the flux tube with the photosphere form pores, sunspots, and faculae, with a concentrated leading region and a more dispersed trailing part (Zwaan 1985). MHD models indeed show that a large-scale flux tube generated in the tachocline can travel through the whole convection zone under the action of magnetic buoyancy (Spruit 1981) and that solar rotation deforms it during its travel, resulting in a more concentrated and more radial flux distribution in the leading part of the active region than in its trailing part, as observed (Caligari et al. 1995 and references therein). Emonet & Moreno-Insertis (1998) have shown that the flux tube must have a certain twist in the convection zone to maintain its coherency during its rise, because magnetic tension tends to prevent the disruption of the flux tube by vertices that form in its wake because of strong shear flows on the tube edges. Recent 2.5-dimensional MHD models that couple the subphotospheric region and the corona show that when the twisted flux tube reaches the photospheric layer, its passage through smaller and smaller pressure scale heights and its arrival in a convectively stable layer tend to decelerate its upward motion, to flatten its upper parts (leading to nearly uncurved and horizontal magnetic fields), and eventually to stop its emergence, which in fact only continues because of the development of a magnetized Rayleigh-Taylor instability (Parker 1966) in the upper parts of the flux tube (Magara 2001).

Unfortunately, in MHD calculations the whole flux tube never emerges: Magara (2001) shows in 2.5 dimensions that after some time, small-scale spatial undulations develop in the photosphere that eventually stop the Parker instability and thus the emergence, because magnetic tension locally balances the buoyancy. The situation seems less dramatic in three dimensions, but even there, Magara & Longcope (2001) and Fan (2001) show that the bottom of the flux tube never emerges because of the very dense material that is trapped in the dipped portions of the magnetic twisted field lines. In both cases, the question that finally arises is how can dipped field lines (also called U-loops) emerge through the photosphere?

The objective of this paper is to address this question by analyzing some data obtained from the balloon-borne Flare Genesis Experiment (FGE) during the emergence of a young active region. Using the same FGE data set, Georgoulis et al. 2002 (hereafter GRBS02) and Bernasconi et al. (2002) have shown that many small-scale, intermittent Hα brightenings, called Ellerman bombs (EBs), occurred during the emergence phase. They analyzed their relationship with the underlying

---

[1] Also at Institute of Theoretical Astrophysics, University of Oslo, Blindern, N-0315 Oslo, Norway.

photospheric magnetic field, and they proposed two triggering scenarios for EBs implying reconnection. In this paper, we pursue the analysis of these EBs with a calculated three-dimensional magnetic field model, and we address the following three issues: What is the magnetic topology of EBs? Can EBs be sympathetically linked to one another, and why? What is their relation with the flux emergence on the larger scale of the active region?

Here we recall what EBs are, and we briefly review the current understanding of their physical processes. EBs (Ellerman 1917), also known as moustaches because of the shape of their spectral profile in Hα, are small intermittent brightening events that are observed in Hα wings (1–10 Å) within young emerging active regions, in particular around their sunspots and under their growing AFSs. EBs have a typical length of ∼1″ (Kurokawa et al. 1982), are commonly elongated (their dimensions are 1″.1 × 1″.8), and are associated with photospheric downflows. Their loci follow the transverse mass flows on the photosphere (GRBS02). Their lifetime depends on the observation cadence, but Qiu et al. (2000) have shown that their brightening lasts about 10–20 minutes. EBs can sometimes be associated with chromospheric surges and with parasitic polarities whose vertical magnetic field is opposite in sign to the larger scale surrounding magnetic field (Rust 1968). EBs are also observed in other wavelengths: in 3840 Å as bright features in the network (Vorpahl & Pope 1972) and in 1600 Å; the latter observations are all well correlated with Hα EBs (Qiu et al. 2000; GRBS02). These events occur at the temperature-minimum region, which is at a small height difference (∼100 km) from the location of EBs. GRBS02 recently found that EBs occur in clusters that exhibit fractal properties, and their typical parameters obey power-law distribution functions, as in case of flare events, with an index of approximately −2.1 in the case of EBs. The total energy of a typical EB is estimated in the range $[10^{27}, 10^{28}]$ ergs, which indicates that EBs are subflaring events, and their temperature enhancement in the radiative volume is $\sim 2 \times 10^3$ K. The mechanism of formation for EBs is still controversial. Different possibilities have been proposed, based on the existence of individual flux tubes with funnel effect (Kitai & Muller 1984) and magnetic reconnection. About the latter mechanism a first question comes up: where does the magnetic reconnection occur? In a reconnection model in the high corona, EBs would be associated with increases of temperature in the corona, but they are not observed. Hénoux et al. (1998) proposed that at the reconnection site, there is a strong emission of particles whose impact with the low chromosphere leads to heating of its dense plasma. More recently, Chen et al. (2001) have presented numerical simulations of magnetic reconnection occurring in the deep atmosphere, based on a previous work by Li et al. (1997) on magnetic reconnection in a weakly ionized plasma. Litvinenko & Somov (1994) have proposed the occurrence of magnetic reconnection at the temperature minimum in the case of the formation of prominences. GRBS02 have shown that EBs occur and recur in preferential locations in the low chromosphere, mostly above, but also in the absence of, photospheric neutral lines. GRBS02 have presented different possible scenarios showing how magnetic reconnection could occur in different magnetic configurations, either in separatrices associated with field lines tangential to the photosphere on the edge of neutral lines—defined in this paper as "bald patches" (BPs; Titov et al. 1993)—or at the interfaces of different magnetic flux systems separated by quasi-separatrix layers (defined in Priest & Démoulin 1995 and Démoulin & Priest

1997). Bernasconi et al. (2002) studied peculiar moving dipolar features, using data from the FGE, as well. They proposed a U-loop model around the moving dipolar features, with emerging flux ropes still tied to the photosphere by trapped dense plasma.

The plan of the paper is as follows. In § 2, we describe the treatment that we applied to an FGE vector magnetogram and the modeling procedure to calculate the magnetic field above the photosphere. In § 3, we calculate the magnetic topology around EBs, and we statistically analyze the relations between the observed EBs and BPs (calculated from either the observed vector magnetogram or the extrapolated magnetic field) and the calculated magnetic separatrices. We then describe a reconnection scenario for EBs that is consistent with the observations. In § 4, we analyze the magnetic connections between various EBs. Through the model we provide evidence for the occurrence of several long, serpentine flux tubes, and we analyze their hierarchical organization with altitude. In § 5, we discuss the results in the frame of large-scale flux emergence through the photosphere. Section 6 provides a summary of the whole paper.

## 2. FROM PHOTOSPHERIC VECTOR MAGNETIC FIELDS TO CORONAL FIELDS

The data used in this work were collected during the 2000 January FGE flight (Bernasconi et al. 2000, 2001). FGE is a balloon-borne 80 cm Cassegrain telescope with an f/1.5 ultralow-expansion glass primary mirror and a crystalline silicon secondary mirror. The observations were obtained through a polarization analyzer unit to give the four Stokes parameters in the red and blue wings of the Ca I line at 6122.2 Å. Unpolarized observations were sequentially obtained at 0.8 Å in the blue wing of the Hα line at 6562.8 Å.

NOAA Active Region (AR) 8844 appeared on 2000 January 23, and rapid growth of emerging flux in its center was observed early on 2000 January 25, characterized by fast-moving mixed polarities with a horizontal flow of 0.3–0.8 km s$^{-1}$ (Bernasconi et al. 2002). FGE observed NOAA AR 8844 on January 25 between 15:50 and 19:16 UT. It obtained 55 vector magnetograms, 28 Dopplergrams of the photosphere, and 28 Hα 0.8 Å filtergrams of the low chromosphere. The FGE magnetograms were calibrated by comparing the longitudinal and transverse fields with the magnetic field maps obtained by the Imaging Vector Magnetograph (IVM; Mickey et al. 1996). Extended information about the data acquisition, the data reduction, and the resolution of the 180° ambiguity can be found in Bernasconi et al. (2002). Schmieder et al. (2004) have used these data, as well as *Yohkoh* (Tsuneta et al. 1991), *Solar and Heliospheric Observatory* (*SOHO*; Scherrer et al. 1995), and *Transition Region and Coronal Explorer* (*TRACE*; Handy et al. 1999) observations, in order to provide a unified scenario of the magnetic evolution and the energy released in this active region. In the following we only focus on a data set corresponding to a snapshot of the evolution of the active region. We use the magnetogram taken at 17:52 UT and the Hα filtergram taken at 17:56 UT.

### 2.1. Reconstruction of the Photospheric Vertical Field

The FGE magnetic vector data are given in the observer coordinate system: the longitudinal field gives the strength of the magnetic field along the line of sight, the zenith angle is the angle between the field vector and the line of sight, and the azimuth angle gives the direction of the projection of the field

vector on the plane perpendicular to the line of sight. In order to extrapolate the magnetic field above the active region, we need to know the magnetic field vector, expressed in the heliographic system of coordinates. Extrapolations often use the longitudinal field as a boundary condition, but the vertical field is essential to determine where there are structures such as fields tangent to solar surface.

On 2000 January 25, NOAA AR 8844 was located at N5° E30°, and the solar disk center longitude was S5°.5. The FGE images must be rotated by 62° counterclockwise with respect to the heliocentric reference system. Thus, the reference system transformation matrix $\mathcal{M}$ (Gary & Hagyard 1990) to pass from the FGE image reference system to the heliospheric reference system is

$$\mathcal{M} = \begin{pmatrix} 0.36 & -0.79 & -0.50 \\ 0.85 & 0.50 & -0.17 \\ 0.38 & -0.36 & 0.85 \end{pmatrix}. \tag{1}$$

It appears that the normal field distribution is more complex than the longitudinal one in the interspot area. This is partly due to the fact that the normal field takes into account the transverse field, which is noisier than the longitudinal field. Nevertheless, near the leading spot, the normal field magnetogram presents some small-scale polarity reversals that are above the normal field noise threshold. These polarities, which were not conspicuous in the longitudinal magnetograms, will be important for the comparison of the modeled field topology with the EBs located in this region.

The FGE field of view is relatively small ($\sim$92$''$) and does not contain the entire flux-balanced magnetic configuration of the active region. This limitation forbids the use of the FGE magnetogram alone as boundary conditions for a magnetic extrapolation. Since the FGE calibration procedure uses IVM magnetograms as a reference (Bernasconi et al. 2002), we included the FGE normal magnetogram in a larger IVM longitudinal magnetogram taken the same day at 18:00 UT (8 minutes later than the FGE magnetogram). It allows us to have a larger field of view with a very small spatial scale and the normal component of the field vector in the center of the active region, where the flux emergence takes place. This composite magnetogram is used for extrapolation in § 2.2. Because our extrapolation code only accepts a limited input data size, we had to rebin the image; thus, our new magnetogram has a typical pixel size of 0.31 Mm (the original FGE pixel size is 0.13 Mm). This is still lower than the FGE actual spatial resolution, which is 0.36 Mm for magnetograms.

## 2.2. *Extrapolation*

We used the linear force-free approximation to extrapolate the field with the Fast Fourier Transform (FFT) method (Alissandrakis 1981; Démoulin et al. 1997). In this approximation the equation for the field is

$$\Delta \boldsymbol{B} + \alpha^2 \boldsymbol{B} = 0, \tag{2}$$

where $\alpha$ is the force-free parameter, assumed to be constant in the entire region. Using the vertical magnetic field as the boundary condition, we calculate the three-dimensional linear force-free magnetic field in the active region atmosphere. For the extrapolation, the vertical magnetogram is included in a box with $L_x = L_y = 160$ Mm and $L_z = 60$ Mm ($z = 0$

corresponds to the photosphere, and the center of the box corresponds to the center of the active region). The Fourier transform is done using $n_x = n_y = 1024$ points. The results are saved on a nonuniform mesh with $n_x = n_y = 401$, $n_z = 60$, with cell sizes (in Mm) varying from (0.25, 0.25, 0.02) to (0.6, 0.6, 5.6). The size of the cell in the center of the active region is sufficiently small to resolve the small-scale polarities observed.

For this size of the box the maximum $|\alpha|$ we can use to ensure that the field is asymptotically null with increasing height is

$$|\alpha_{\max}| = \frac{2\pi}{L_x} = 3.92 \times 10^{-2} \text{ Mm}^{-1}. \tag{3}$$

Here $\alpha$ is the free parameter of our extrapolation. It is chosen so that the electric currents of the extrapolation best fit the active region real electric currents. We used two ways to find $\alpha$:

1. We first compared the extrapolated and observed horizontal fields (the component of the field tangential to the photosphere, at the level of the photosphere). We selected the value of $\alpha$ for which the orientation of the extrapolated horizontal field best matched the orientation of the observed horizontal field, especially in the interspot region. The comparison was restricted to horizontal fields stronger than 200 G (well above the noise threshold). Figure 1 compares the observed horizontal field with the best-fit extrapolated one. The differences between the observations and the extrapolation can be explained by different facts: in the observations there may be a relatively important error on the azimuth angle—and consequently for the tangential field—in weak-field regions. Bernasconi et al. (2002) gives an average error of 12°.2 for a transverse field of 200 G. For extrapolation, our code assumes periodic boundary conditions, which induce a multipolar environment on large scales that modifies the field topology, especially near the sides of the box. The extrapolated horizontal field best matches the observed one for a force-free parameter $\alpha_f$:

$$\alpha_f = 2.2 \times 10^{-2} \text{ Mm}^{-1}. \tag{4}$$

In order to confirm this value, we have used an algorithmic method (the minimum residual method described in Leka & Skumanich 1999) to compute the value of $\alpha$ that minimizes the difference between the FGE observed horizontal field and the horizontal field extrapolated using the IVM longitudinal magnetogram. This method gave an $\alpha$ equal to $2.07 \times 10^{-2}$ Mm$^{-1}$, which is only 7% less than the value we found with the FGE magnetograms.

2. Then we tried to fit the low EUV loops of *TRACE* with some extrapolated field lines computed with the force-free parameter $\alpha_f$ (see Fig. 2). Matching field lines with observed EUV, X-rays, or H$\alpha$ loops is a common method used to constrain the force-free parameter (see, e.g., Schmieder et al. 1997). Since EUV loops are structures located in the corona, this method tends to give an accurate extrapolation of the magnetic field above the photosphere. Because we focus on low-lying magnetic features in the following, we used this method only secondarily. Looking at the horizontal field first, we make sure that the force-free value we use gives a good fit to low fields. However, with $\alpha_f$, we see that the *TRACE* loops can be very well fitted by field lines in the center and in the southern part of
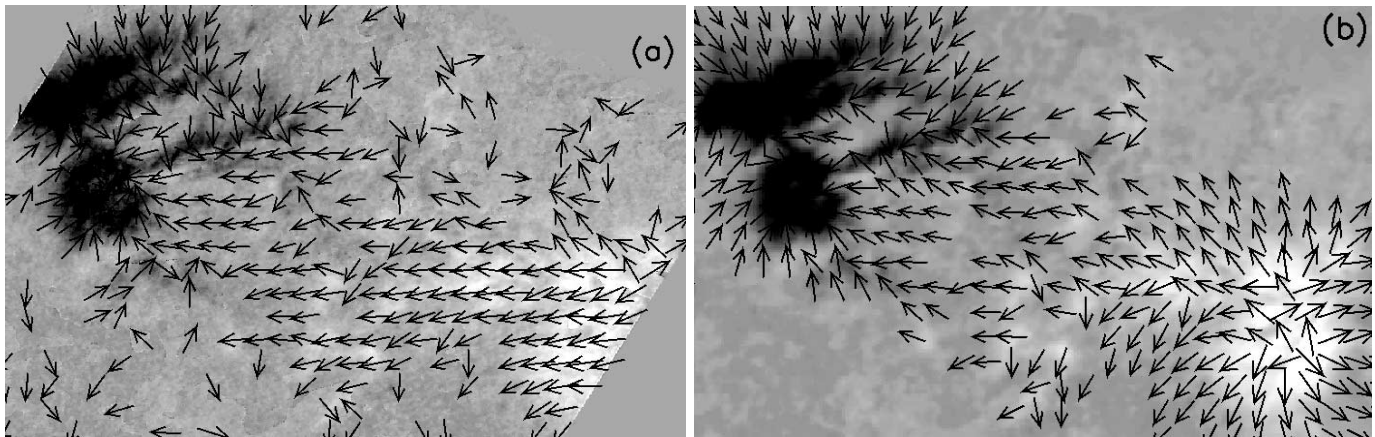
Fig. 1.—(a) Observed horizontal field. The background image is the $B_z$ magnetogram, as deduced from the FGE magnetogram. (b) Extrapolated horizontal field on the vertical field magnetogram used as an input in the extrapolation. One notes the inclusion of the FGE magnetogram in the IVM magnetogram. In both panels the arrows give the orientation of the horizontal field, and their length is proportional to the logarithm of the field amplitude. These arrows are only plotted in regions where the total field is stronger than 200 G.

the active region. Schmieder et al. (2004) have shown that the highest loops and the northern loops of the region were best fitted with a lower parameter: $\alpha = 9.4 \times 10^{-3}$ Mm$^{-1}$. This shows that the hypothesis that the whole region has the same twist is not perfectly true, which is not surprising, since $\alpha$ is strictly constant only along a field line. Schmieder et al. (1996) had already pointed out the existence of a gradient in the magnetic shear above an active region. But since the lines computed with $\alpha_f$ fit well the central low loops, where our study takes place, we keep this value of the twist for the following.

We wish to point out that the linear force-free field (LFFF) approximation may not a priori give a good representation of the magnetic field at low altitudes: in the photosphere and chromosphere, pressure and gravity can substantially modify a

force-free field, since $\beta \sim 1$. Linear magnetohydrostatic models could have been computed, but we did not use them for two reasons: first, Aulanier et al. (1998) have shown that these models did not significantly affect the BP topologies; second, we wanted to highlight purely magnetic effects. In this context, nonlinear force-free field models should be used. But we chose to restrict ourselves to the linear approximation because of the strong efficiency of the Fourier transform method in dealing with the very small-scale features that we are interested in, as opposed to numerical finite-difference methods that are required to compute nonlinear models, which typically require many more grid points than we used and have never been tested at this high spatial resolution and with BP topologies (see, e.g., Régnier et al. 2002 for an application to large-scale coronal structures).
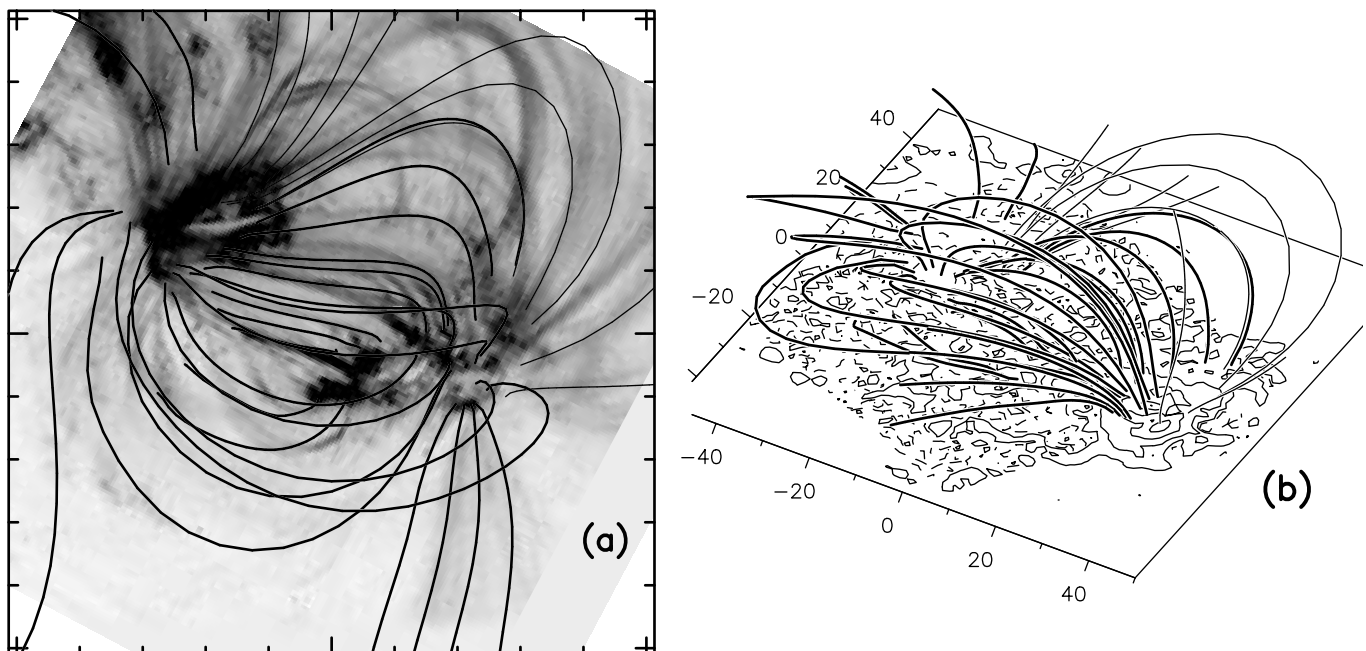


Fig. 2.—(a) Extrapolated field lines on a *TRACE* image (inverse color table) taken at 171 Å on 2000 January 25 at 18 : 02 UT. The thick lines fit the *TRACE* loops best. (b) Projection view of the extrapolated field lines. On the base plane, the thin solid (dashed) lines represent isocontours of the vertical component of the magnetic field of 50, 300, 900, and 1800 G positive (negative) values.

## 3. ELLERMAN BOMBS AND MAGNETIC TOPOLOGY

### 3.1. *Bald Patches*

Separatrix surfaces are locations where current layers might be formed, and thus where reconnection can take place. Classically, a separatrix is a three-dimensional surface defined by all the field lines passing through one null point. If there are no null points, another class of separatrix can be considered: they are defined by field lines passing through BPs (Titov et al. 1993). BPs are regions where the vector field is tangent to the boundary (photosphere) along a magnetic inversion line. On a BP the field line curvature must be positive, so a BP is a region of the photosphere ($z = 0$) where

$$B_z = 0 \quad \text{and} \quad \boldsymbol{B} \cdot \nabla B_z > 0. \tag{5}$$

If the field satisfies the above condition at a point above the photosphere, this point is called a magnetic dip.

The separatrix field lines passing through these BPs are likely sites for magnetic reconnections (see, e.g., Low & Wolfson 1988). This issue has been disputed by Karpen et al. (1991), who have shown that the thickness of the low chromosphere can prevent thin current sheets from forming in such configurations. But Billinghurst et al. (1993) have explained why strong currents can still develop—at least—near the footpoints of the separatrix, because of the strong concentration of the flux tubes in these regions. In addition, Delannée & Aulanier (1999) provided analytical arguments in favor of current sheet formation right above BPs, since gravity can result in a quasi–line tying in a concave field line located in a photosphere that is denser than the atmosphere considered in Karpen et al. (1991). Finally, extrapolated BPs have already been related to various types of observed flares (e.g., Aulanier et al. 1998; Fletcher et al. 2001; Mandrini et al. 2002; Wang et al. 2002), which adds observational evidence in favor of reconnection along BP separatrices. In this frame, we wish to compare the EB positions with BPs and separatrix footpoint positions.

### 3.2. *Ellerman Bomb–Bald Patch Correlation*

The Hα observations reveal the occurrence of numerous EBs in the interspot region of NOAA AR 8844. In order to determine how many EBs can be found in the 17:56 UT Hα filtergram, two simple methods can be used. GRBS02 relied on the contrast, $I_c(\boldsymbol{x}) = [I(\boldsymbol{x}) - I_0]/I_0$, calculated for each location to identify individual EBs: $I(\boldsymbol{x})$ is the intensity of a pixel with vector position $\boldsymbol{x}$ and $I_0$ is the background mean intensity averaged over the whole field of view. An EB is considered to exist where the contrast is above a fixed threshold. At 17:56 UT, one can detect six EBs for a threshold of 0.08 (i.e., the intensity of the EB must be at least 8% above the background). For a threshold of 0.04, 38 EBs can be detected.

But the mean threshold value method tends to neglect EBs that could occur where the local background is darker than the mean background. These EBs would create a local enhancement of brightness, but if the intensity is not above the threshold, these EBs would not be detected. We finally consider 47 EBs with the local contrast enhancement method. For these EBs the contrast with the local background is above 0.04, using a definition similar to that for the mean threshold method.

In Figure 3*a*, we first compare the EB position with the BPs directly computed using the observed vector field ($B_x, B_y, B_z$)

(we refer to these BPs as "observed BPs" in the following). The BPs are computed on a mesh whose typical cell size is 0.1 Mm, which is smaller than the field data resolution. For the computation of BPs the field is linearly interpolated between cells of the extrapolation. Then, in Figure 3*c*, we compare the EB locations with BPs computed from the extrapolated field (these BPs are named "extrapolated BPs"). The extrapolated and observed BPs are only computed in regions where the tangential magnetic field is stronger than 200 G, well above the noise threshold, to improve the signal-to-noise ratio.

There are some differences between these two figures (Figs. 3*a* and 3*c*). Figure 3*a* presents a sparser distribution of BPs than Figure 3*c*. This is mainly due to the fact that when we compute the BPs directly from the observation the magnetogram pixel size is half that of the extrapolated magnetogram. The BP distribution given by the extrapolation is thus smoother than the one obtained directly from observations. Despite this difference, the location of the large groups of BPs is in a rather good agreement between the extrapolation and the observation.

In Figure 3*b*, we can see that 35 out of 47 EBs (74%) are associated with observed BPs. We only associate an EB with a BP if both are strictly cospatial. The typical velocities of horizontal motions being ≤1 km s$^{-1}$, the plasma could have moved about 0.24 Mm during the 4 minutes that separate the Hα image and the magnetograms, which is less than the spatial resolution of the Hα image (which is 0.58 Mm). Thus, only a BP located in the emission area of the EB can be linked to this EB. That is why we decided not to associate the bright EB in the center of the rectangle in Figure 3*c* with the really close BPs. Figure 3*d* shows that 23 EBs coincide with extrapolated BPs. The observed and extrapolated BPs disagree for 16 EBs (i.e., the EBs that are related to either observed or extrapolated BPs).

In these figures, one can notice the existence of some BPs near the leading spot, in the region delimited by a rectangle in Figure 3*a*. These BPs are due to the presence of small negative polarities that were not present in the longitudinal field. More interesting is the fact that some EBs are located on some of these BPs. Using line-of-sight vector magnetograms, GRBS02 supposed that the EBs located in this region were triggered by the interaction of two topologically different, unipolar, magnetic configurations (see Fig. 12*c* in GRBS02). One can see that the use of heliographic magnetic field components may explain the triggering of some of these EBs by the same mechanism as for the EBs located in the interspot region.

By computing the observed BPs at three other times, we have found some similar results, which are presented in Table 1. The first column gives the times of the Hα filtergrams. The time of the vector magnetograms is given in the second column. The third column indicates the total number of EBs detected for each Hα image, and the fourth column gives the number of EBs that can be spatially related to BPs directly computed with the magnetograms. The fifth column gives the ratio of the number of EBs that can be linked with observed BPs to the total number of EBs. The spatial correlation between the EBs and the BPs directly computed from the observation is always between 70% and 75%.

### 3.3. *Ellerman Bomb–Separatrix Footpoint Correlation*

With the extrapolated field it is possible to compute the separatrices associated with the extrapolated BPs. The latter are shown in Figure 4*a*. Thus, we can compare the EB positions
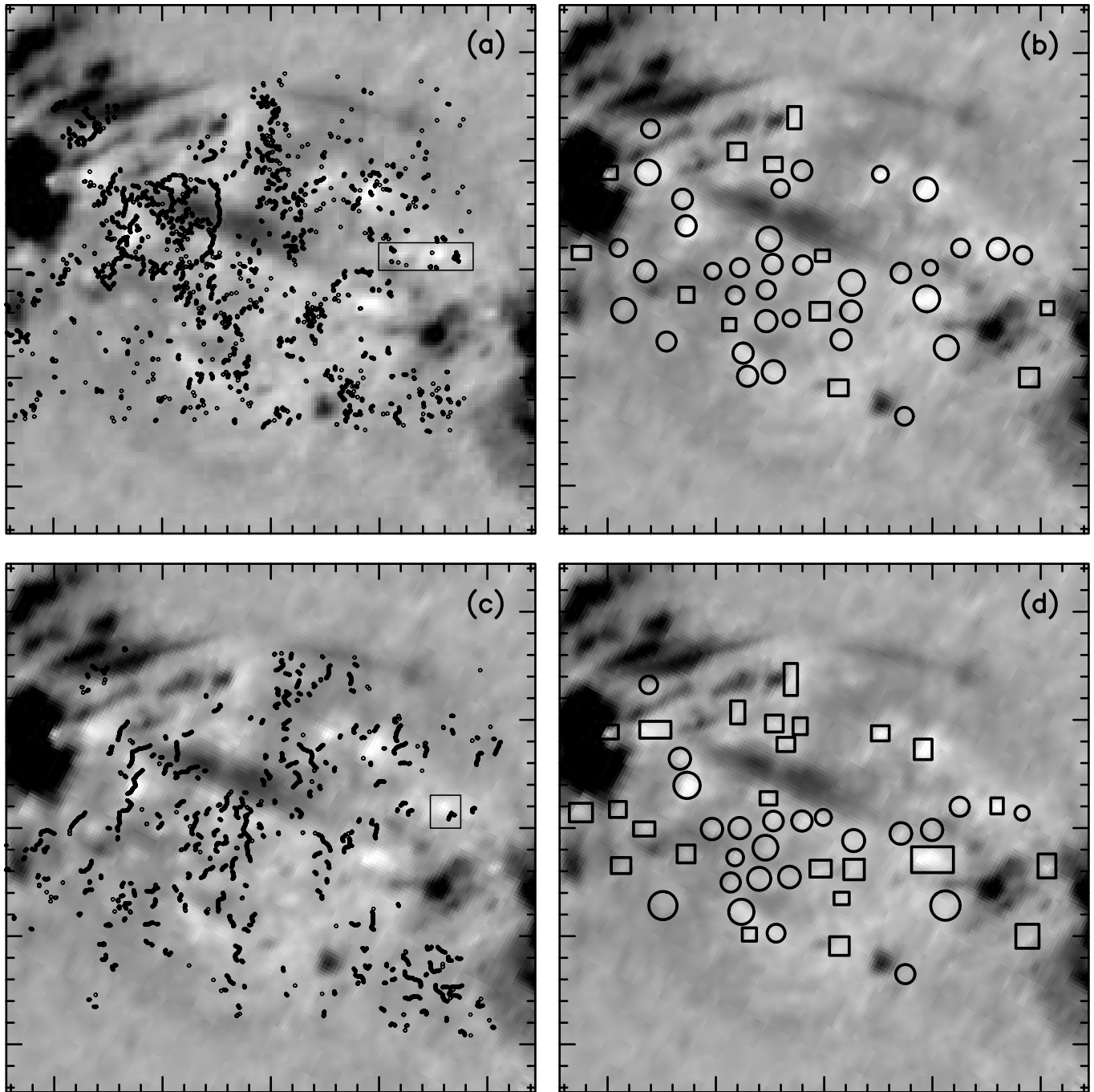
FIG. 3.—*Background*: The 17:56 UT FGE Hα 0.8 Å image. See § 3.2 for the EBs located in the rectangles. (*a*) Observed BPs (*dots*), directly computed from the observed full vector field. (*b*) Correlation between EBs and observed BPs. The 35 circles represent the EBs that coincide with a BP directly computed from the observation, and the 12 squares show EB locations were no BP can be found. (*c*) Extrapolated BPs (*dots*) computed with the extrapolated field. (*d*) Correlation between EBs and extrapolated BPs. The symbols are the same as in (*b*): 23 circles and 24 squares.

TABLE 1

EBS ASSOCIATED WITH (⇔) OBSERVED BPS ON 2000 JANUARY 25

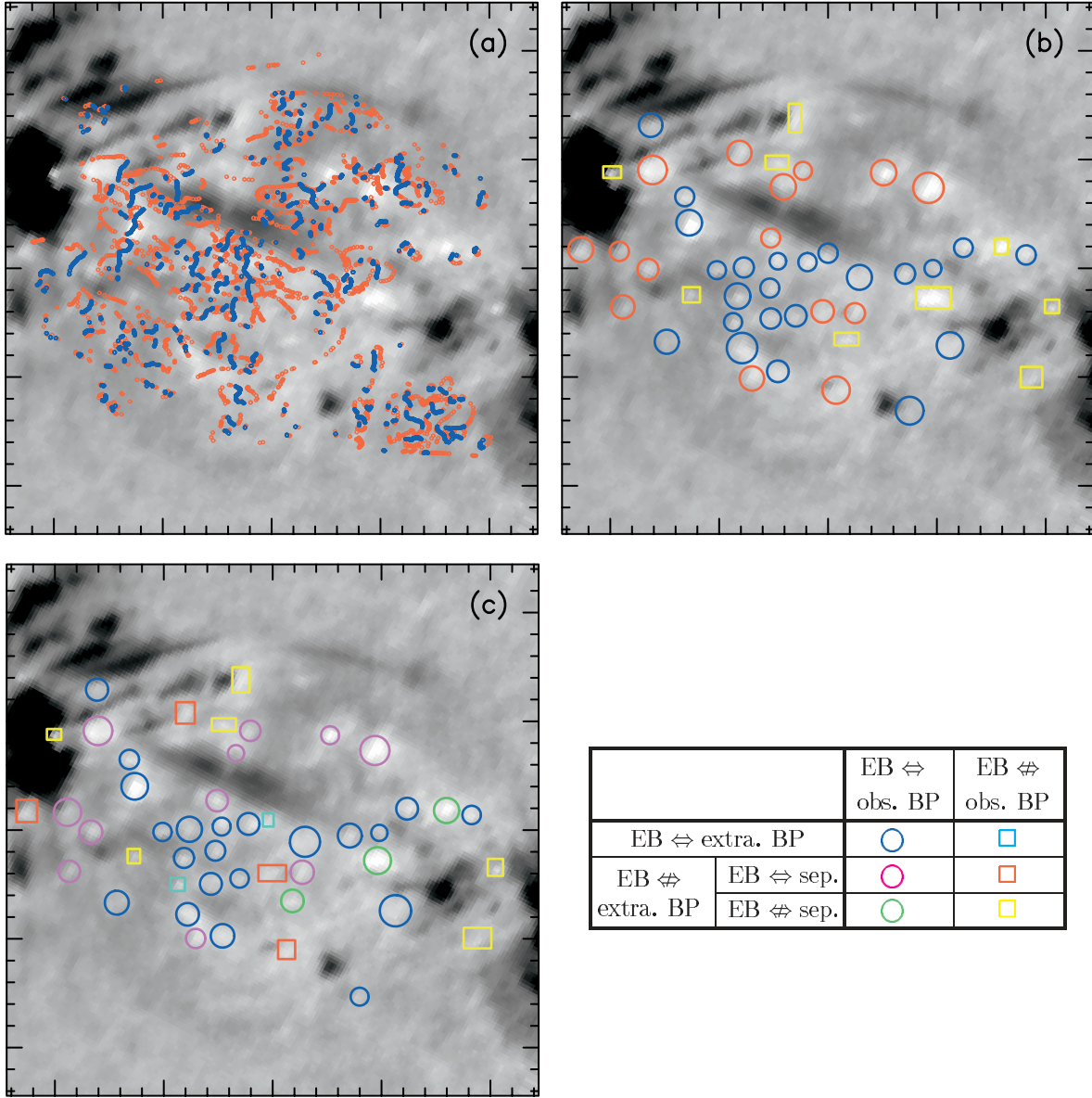| Hα Filtergram (UT) | Magnetogram (UT) | Total EBs | EBs ⇔ Obs. BPs | (EBs ⇔ BPs) / Tot. EBs (%) |
|---|---|---|---|---|
| 16:25 ............................ | 16:27 | 40 | 28 | 70 |
| 16:47 ............................ | 16:49 | 44 | 33 | 75 |
| 18:49 ............................ | 18:50 | 42 | 31 | 74 |
| 17:56 ............................ | 17:52 | 47 | 35 | 74 |

NOTE.—Obs. BPs: observed BPs.

Fig. 4.—*Background*: The 17:56 UT FGE Hα 0.8 Å image. (*a*) Extrapolated BPs (*blue dots*) and the footpoints of the field line passing by these extrapolated BPs (*red dots*). (*b*) Correlation between EBs, extrapolated BPs, and the separatrix footpoints associated with the BPs. The 23 blue circles represent the EBs associated with (⇔) extrapolated BPs (see the circles in Fig. 3*d*); the 15 red circles are for the EBs that can be associated with separatrix footpoints; the nine yellow squares are for the EBs not associated with any special magnetic feature. (*c*) Synthesis of the three previous BP computations: the 21 blue circles are for the EBs related to BPs in both the observations and the extrapolation; the three green circles are for the EBs that can be associated with an observed BP but with no extrapolated magnetic features; the 11 pink circles are for the EBs that coincide with an observed BP and the footpoint of an extrapolated separatrix (but not to any extrapolated BP); the two light blue squares are for the EBs related to extrapolated BPs but not to observed BPs; the four red squares are for the EBs linked only with footpoints of extrapolated separatrices (and not to any observed or extrapolated BP); the six yellow squares are for the EBs that can be associated with no observed or extrapolated special magnetic feature.

with the positions of the extrapolated BPs and the locations of the footpoints of the associated separatrices, which are preferential sites for reconnection. Among the 47 EBs that we selected, 23 are on extrapolated BPs. Among the 24 remaining EBs, 15 are located near the footpoints of separatrices associated with BPs. Only nine EBs (less than 20%) are not related to any specific topological magnetic feature.

To assure ourselves that our results about the correlation between magnetic features and EB are not coincidental, we compared the distribution of extrapolated BPs and separatrix footpoints with random distributions of EBs (a so-called Monte Carlo test). We created 30 artificial Hα images. Each

image contains 47 EBs randomly distributed in the interspot region whose area is the same as the mean area of the real EBs ($1.''1 \times 1.''8$; see GRBS02). For random distributions of EBs, we found that on average 30% of EBs can be associated with extrapolated BPs, only 20% can be associated with separatrix footpoints, and 50% cannot be linked with any magnetic feature. Even in the case that gives us the strongest correlation between random EBs and extrapolated magnetic features, we did not reach the value of 80% correlation that we obtained between extrapolated BPs and Hα observations. The same kind of Monte Carlo test has been made for the observed BP distribution. With 47 randomly distributed EBs, an average of

TABLE 2
SUMMARY OF EB CORRELATIONS

| Category | Total | EBs ⇔ Obs. BPs | EBs ⇎ Obs. BPs |
|---|---|---|---|
| All EBs ........................ | 47 | 35 | 12 |
| EBs ⇔ extra. BPs........ | 23 | 21 | 2 |
| EBs ⇎ extra. BPs........ | 24 | 14 | 10 |
| EBs ⇔ sep. .............. | 15 | 11 | 4 |
| EBs ⇎ sep. ............ | 9 | 3 | 6 |

NOTE.—Obs. BPs: observed BPs; extra. BPs: extrapolated BPs; sep.: separatrix footpoints. The symbols ⇔ and ⇎ mean "associated with" and "not associated with," respectively.

23 EBs (50%) are cospatial with observed BPs, which is significantly less than the result given with the observations.

In Figure 4c and Table 2, we summarize the results of the previous BP and separatrix computations. Among the 16 EBs for which there was a disagreement between the two methods we used (observation and extrapolation), one can see that 11 EBs that could be associated with observed BPs but not with extrapolated BP can be linked with separatrix footpoints in the extrapolation. That suggests that the lack of resolution in the extrapolated magnetogram may be accountable for this difference, especially if we consider the serpentine field topology described in § 4: a BP that is normally linked to other BPs and is not detected as a BP in the extrapolation will be located really close from a separatrix footpoint.

Only six EBs out of 47 were not related to any kind of BP or separatrix. The lack of relationship between these EBs and any magnetic feature may be due to the difference in time between the Hα image and the magnetograms—4 minutes. This slight mismatch may be due to local strong departures from the LFFF approximation (see § 3.2). Another possibility may be a different reconnection process that does not need the presence of BPs. However, 87% of the EBs (41 out of 47) are directly related to preferential sites of reconnection. This clearly emphasizes the close link that exists between EBs and BP field lines. EBs seem to be subflares associated with BP reconnection sites. Thus, what we present here is strong evidence for reconnection taking place in the low chromosphere.

## 4. SERPENTINE FIELD LINES

### 4.1. *Undulatory Connections*

By studying the photospheric plasma motions in an active region, Strous (1994) showed an area where the plasma presented an interesting pattern: parallel bands, perpendicular to the emerging flux, of successive downflows and upflows. This suggested that the magnetic flux did not emerge in the shape of an Ω-loop, but rather presented some undulations. We studied the magnetic topology of the center of the active region, in order to investigate whether the low field lines present this specific serpentine shape. Because parts of the undulatory field lines must have a U-loop shape typical of the field lines passing through BPs, we computed the separatrix field lines associated with each BP in the active region to see if some of them present a serpentine form, i.e., if some of these field lines are passing through several BPs or low-lying dips.

With the 17:52 UT magnetogram, we identify at least six groups of undulatory flux tubes (or serpentine field lines) connected to several points of the photosphere or low chromosphere ($z < 1$ Mm). Indeed, the serpentine lines often go through dips located in the lower part of the chromosphere, never more than 0.5 Mm high and very often less than

0.2 Mm. In this region $\beta$ is still important, and consequently the magnetic field line motions are due to the plasma motions, as in the photosphere. Metcalf et al. (1995) have shown that in an active region, the field only becomes force-free above 0.4 Mm high. Consequently, the physics of these low-lying dips is very similar to the physics around photospheric BPs.

### 4.2. *Examples of Serpentine Field Lines*

In the following we display three examples of these serpentine field lines—Figures 5, 6, and 7—and show how they are related to other chromospheric features, such as EBs.

Figure 5 presents the first example of an undulatory flux tube. This very flat serpentine line goes through two BPs (BP 1 and BP 2) and two low-lying dips (BP 3 and BP 4). It is 20 Mm long, and its maximum height is 1.3 Mm. Figure 5a shows that this serpentine line is connected to a border of the supergranule (at BP 4) and is also linked to one of the moving dipolar features studied by Bernasconi et al. (2002). In Figure 5b, we can see that BP 2 and BP 4 are located at the exact positions of EBs and that some of their footpoints are over one bright EB near the trailing spot.

In Figure 6, we can see another serpentine field line. This group of field lines is about 30 Mm long and 1.7 Mm in height at its top. The serpentine line goes through two BPs (BP 6 and BP 9) and three dips (BP 5, BP 7, and BP 8). Figure 6b shows that BP 5, BP 6, BP 8, and BP 9 are close to EBs. The footpoints of the BP separatrix (and especially the footpoints near the trailing spot) are on EBs, too.

The third example of undulatory flux shows this close connection between EBs and emergent flux tubes, too. This example is presented in Figure 7. This small serpentine line has one BP (BP 10) and one dip (BP 11). It is 15 Mm long and 2 Mm high. What is particularly striking about this example is the similarity between the shape of the field line and the positions of a series of EBs. In Figure 7b, one can see that BP 10 and BP 11 are located around some EBs that present a V-shape. The serpentine field line has exactly the same V-shape. This clearly emphasizes the close link between EBs and serpentine field lines.

The fact that several EBs cospatial with BPs that are magnetically linked by the same field line might suggest that the EBs can be sympathetically linked. Since the temporal resolution of our data is not sufficient to study the exact temporal triggering of the different EBs located along a unique field line, it is impossible for us to go beyond this suggestion.

### 4.3. *Serpentine Field Line Environment*

Figures 6c, 6d, 7c, and 7d allow us to understand better the magnetic topology in the neighborhood of serpentine lines. All represented lines are separatrix lines, passing through one or several BPs. Under the folds of serpentine lines there are small lines (*yellow lines*) connected to the photosphere by one or two BPs. These lines rarely exceed 5 Mm in length. Over serpentine lines, there are some BP-connected field lines, too (*green lines*). These lines are 20–35 Mm long and 2–10 Mm high and are formed of two very asymmetric lobes. Serpentine field lines are lying under the biggest lobes of these separatrices; that is why we refer to them as "domes" in the following. This complex topology, as shown in Figure 8, is summarized in Figure 9.

## 5. THE NATURE OF FLUX EMERGENCE

As pointed out in § 1, MHD simulations show that the emergence of a magnetic flux tube from beneath the
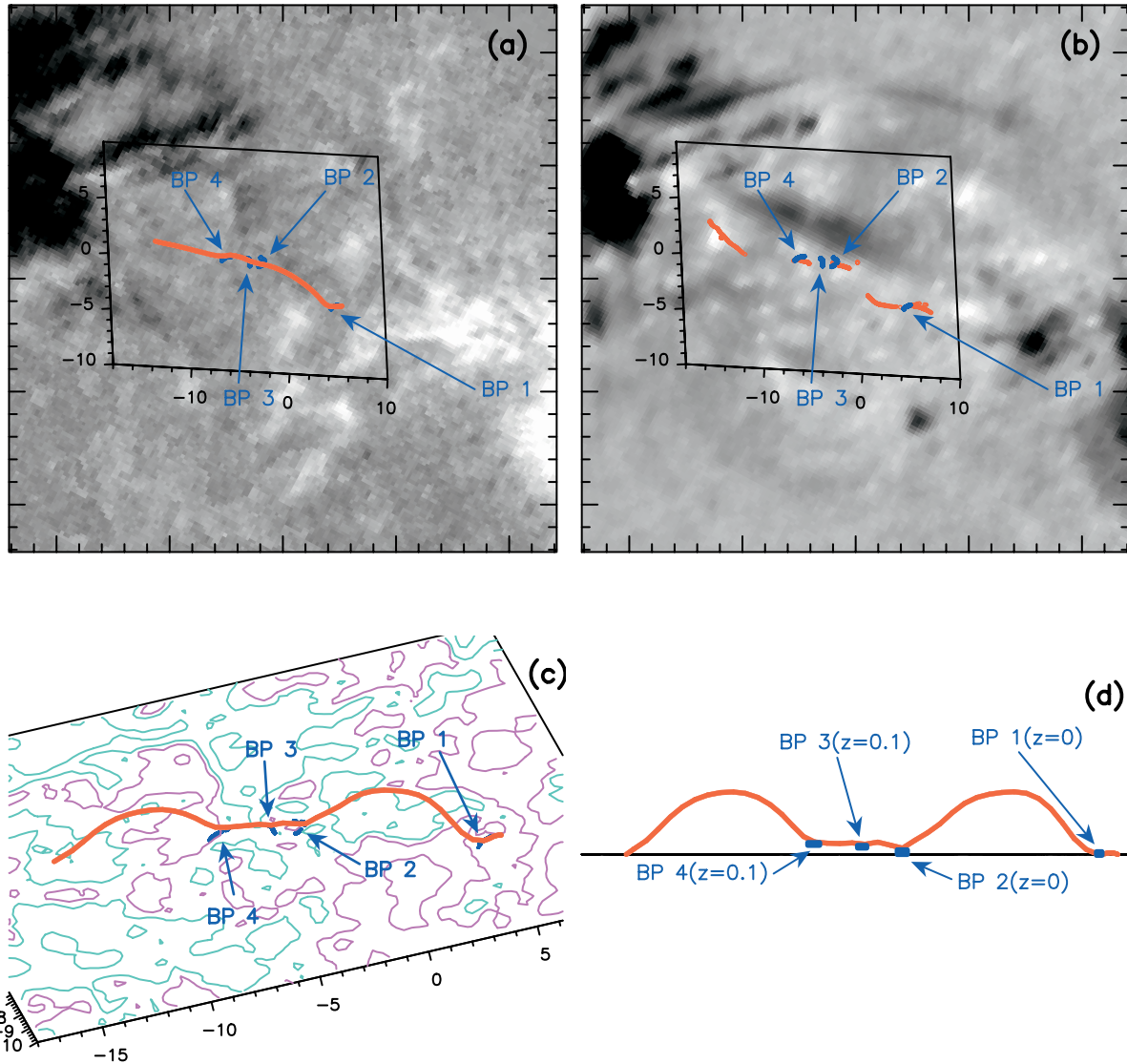
Fig. 5.—First example of an undulatory flux tube: only one field line of the serpentine flux tube (*red line*) is represented on these figures. The blue dots (denoted BP 1–BP 4) represent the BPs and dips through which the serpentine line is passing. (*a*) Position of the undulatory field line on the vertical magnetogram. (*b*) Positions of the footpoints of the serpentine line (*red dots*) on the Hα 0.8 Å filtergram. In (*c*) and (*d*), a multiplicative factor of 3 for vertical extension of the field line is used for a better viewing of the configuration. (*c*) Projection view of the undulatory flux. On the base plane, the isocontours represent $B_z(z = 0) = \pm 50$, 300, 900, and 1800 G, pink for positive and blue for negative values. The base plane boundaries are represented in (*a*) and (*b*). (*d*) Side view of the undulatory field line. The height of the BPs and dips are indicated in Mm.

photosphere is not simple: first, Magara (2001) shows that the emergence stops after some time because the flattened emerging flux tube becomes stable to the Parker instability; and second, Fan (2001) shows that the emergence of the lower (dipped) parts of an emerging twisted flux tube is impossible because of the weight of the subphotospheric trapped plasma. In the following, we explain how our results suggest the way the Sun resolves both these difficulties.

We found a hierarchy of serpentine, undulatory flux tubes located below chromospheric altitudes. This hierarchy can suggest that the field lines located at increasing altitudes represent different stages of a gradual flux emergence. Small arcades separated by BPs gradually rise from the photosphere and form longer and longer arcades when they reach the chromosphere.

They finally rise in the low corona, forming the observed elongated AFSs. Two questions naturally arise from this scenario, which follows from the difficulties addressed above: why do the flux tubes have undulatory shapes at low altitude, and how can they dispose of the dense material trapped in (and below) their photospheric dips (i.e., BPs)?

The answer to the first question lies in the wavelengths of the spatial undulations of the serpentine field lines, which are given by the distances between two BPs taken sequentially along the flux tube. These distances can be typical of either convective scales present between both sunspots of the active region—such as 1 Mm for granulation and 10 Mm for supergranulation—or of some MHD instability. In the first case, convection is the main driver of undulations, whereas in the
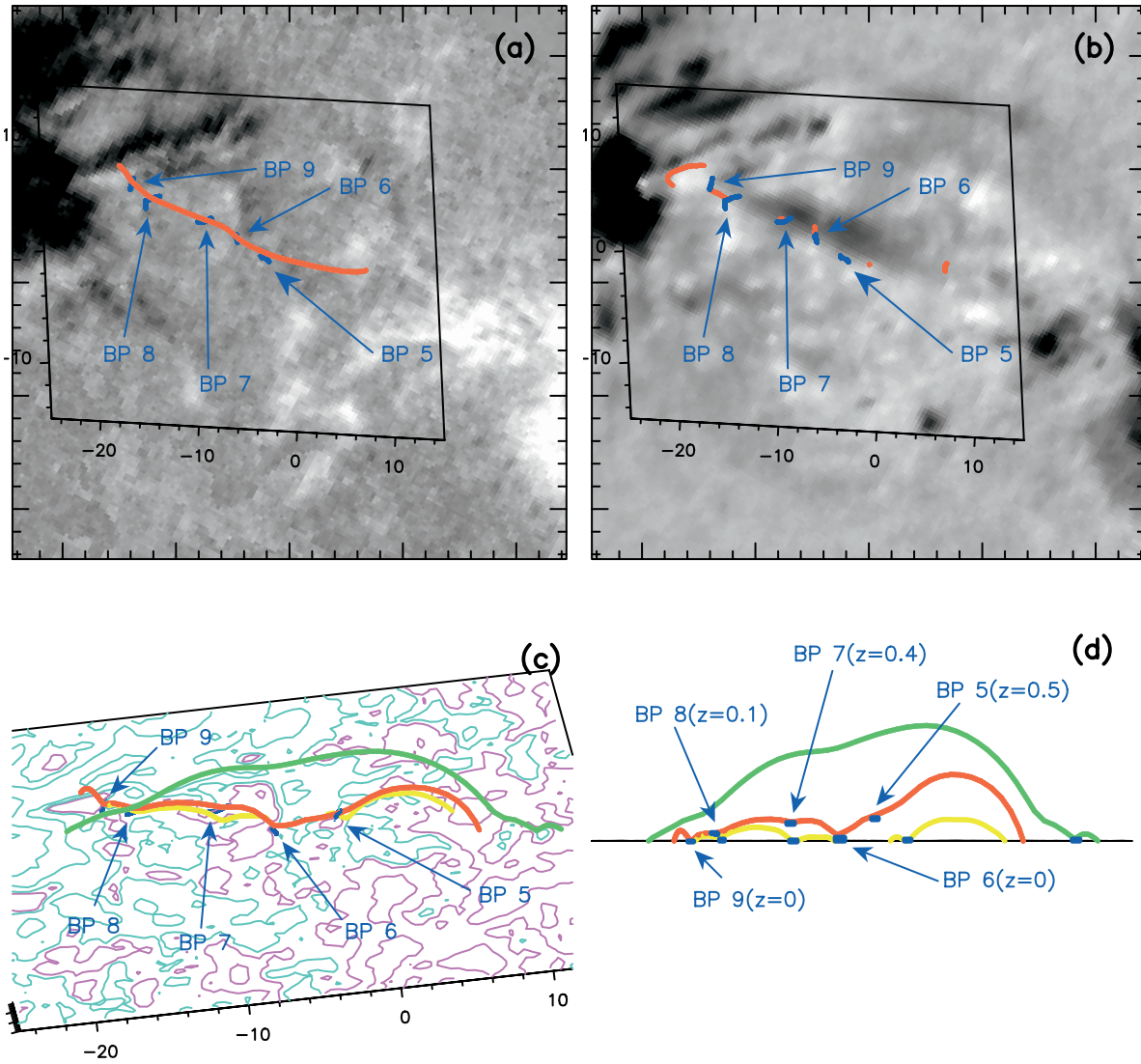
FIG. 6.—Second example of an undulatory flux tube. Panels and symbols are as in Fig. 5. In (c) and (d), in addition to the main serpentine line (*red line*), other field lines passing through BPs are shown: the yellow lines are located beneath each fold of the serpentine line; the green line is above the main serpentine field line.

second case the serpentine shape originates from some insta-bility, which has to be identified. The flux tube must be less dense than the surrounding medium, to ensure that buoyancy made possible its rise through the convection zone (see, e.g., Caligari et al. 1995); in addition, it is probably very flat, with mostly horizontal magnetic fields below the photosphere (Magara 2001). So in the absence of magnetic field, the upper interface between the subphotospheric flux tube and the pho-tosphere should be Rayleigh-Taylor–unstable to any perturba-tion of any wavenumber $k_x$, where $x$ ($z$) is the horizontal (vertical) direction. Qualitatively, this horizontal interface can be stabilized by magnetic forces for perturbations having high $k_x$, resulting in highly curved field lines whose magnetic tension can prevent the instability from developing. Quantitatively, there is a critical wavenumber $k_x^c$ below which magnetic tension is not sufficient to prevent the instability: this is the Parker instability (Parker 1966). The value of $k_x^c$ can be evaluated by linearizing the Euler equation, assuming total pressure balance

and constant temperature between the inner and the outer parts of the flux tube. It gives

$$k_x^c \simeq 1/(2H), \qquad (6)$$

where $H$ is the pressure scale height. These assumptions lead to a result that is independent of the magnetic field amplitude, because the latter is directly related to the density depletion in the flux tube (see, e.g., Magara 2001). Using a typical photo-spheric temperature ($T = 5800$ K), one then finds that un-dulatory flux tubes will be Parker-unstable if their wavelength $\lambda_x$ satisfies

$$\lambda_x > 4\pi H \simeq 2 \text{ Mm}. \qquad (7)$$

Among the six identified serpentine lines in our extrapolation, we measured 29 values for $\lambda_x$, which are plotted in the form
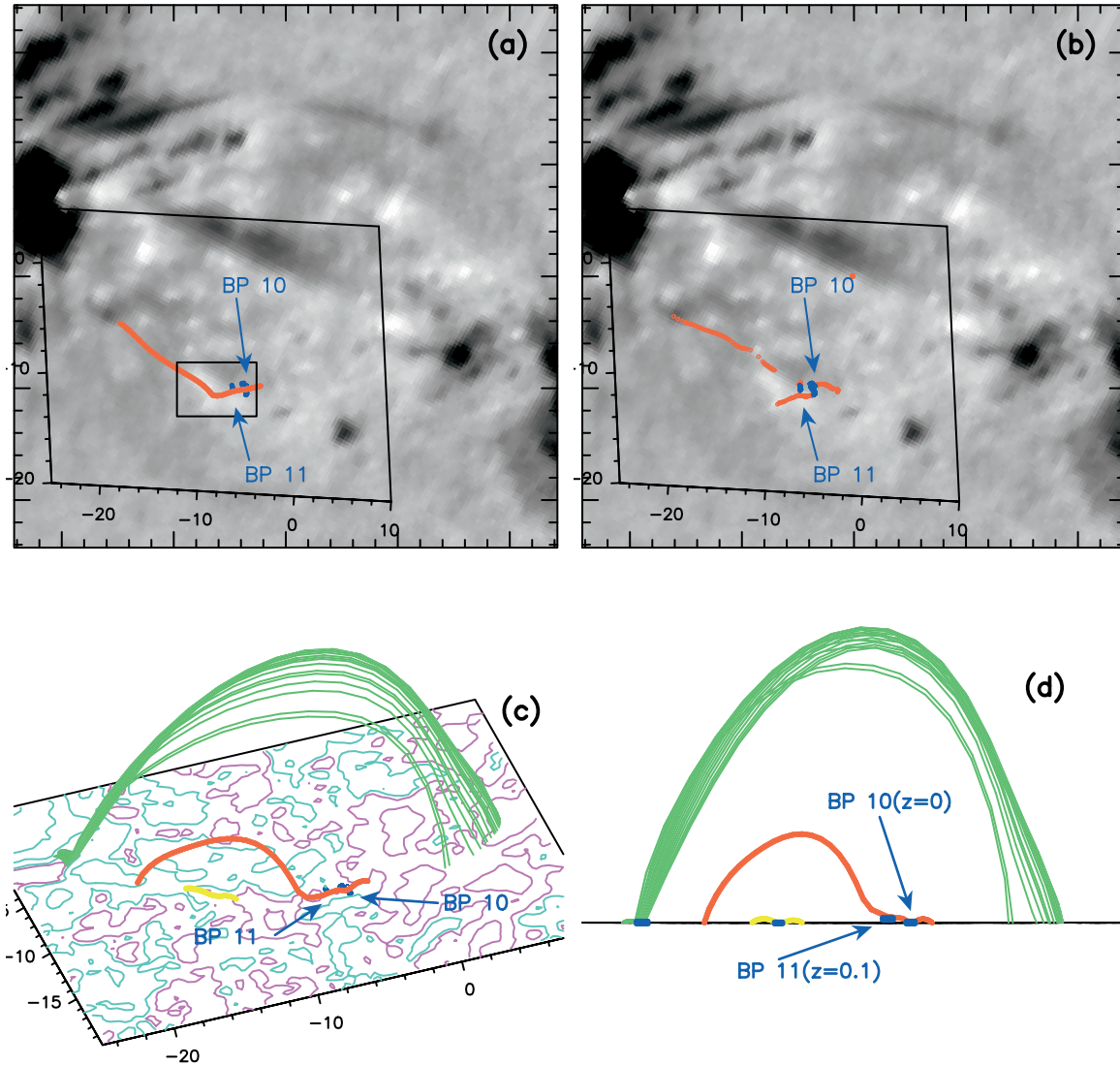
FIG. 7.—Third example of an undulatory flux. Panels and symbols are as Fig. 5, except for (*a*), where the background image is an Hα 0.8 Å filtergram. In the small rectangle one can note the V-shape of the EBs, which matches the shape of the field line.

of a histogram in Figure 10. Even though one small peak is identified around 8 Mm (which is the size of the small supergranule on the eastern side of the trailing sunspot), there is a very clear asymmetric peak around 3 Mm that has a sharp cutoff for values below 2 Mm. This cutoff does not come from a coarse spatial resolution, since the FGE resolution was 0″.5 and the extrapolation was calculated with the FFT on a uniform mesh with 0.16 Mm cell⁻¹ and analyzed on a nonuniform mesh of 0.25–0.42 Mm cell⁻¹ between the two sunspots. Even though the statistics are not absolutely sufficient, this distribution very clearly supports that the Parker instability is at the origin of the emerging undulatory flux tubes, with wavelengths that are larger than those developing in the MHD calculations of Magara (2001) after his flux tube stopped emerging. Our results are then consistent with the persistence of the Parker instability at small scales in the early stages of active region emergence. They are also consistent with the results of Bernasconi et al. (2002), who found that the EBs were associated with moving dipolar features. They show

that a pair of moving features were constantly separated by ∼3 Mm during the whole time of observation.

The answer to the second question is given by the good correlation that we found between EBs and BP separatrices, calculated from either the vector magnetogram or the magnetic field extrapolation. This suggests that impulsive, resistive effects do occur in the photosphere in field lines that have portions tangential to the photosphere, i.e., in field lines having dips that are filled by dense subphotospheric material. The material flows along the serpentine field lines down into the dips. This agrees with the observation of GRBS02 that more than 80% of EBs are associated with downflows. This is also consistent with the results of Bernasconi et al. (2002), who found that the moving dipolar features (which present a BP topology) they studied had a net downflow, whereas the region between the moving dipolar features presents an upflow (see Fig. 9 in Bernasconi et al. 2002).

Even though our work does not address the details and the precise altitude of the resistive effects, the associated magnetic
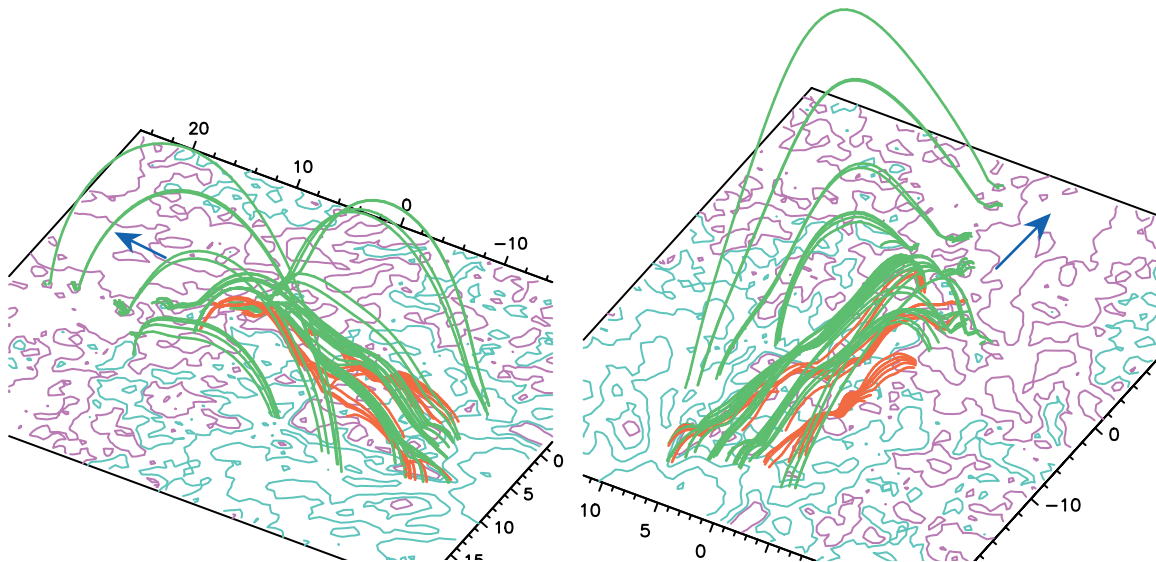
Fig. 8.—Projection view of the serpentine field lines and their surrounding environment in the center of the active region. The red lines represent the serpentine lines presented in Figs. 5 and 6. The green lines represent the domes. On the base plane, the isocontours represent $B_z(z = 0) = \pm 50$ 50, 300, 900, and 1800 G, pink for positive values and blue for negative. The blue arrows mark the direction of the leading spot. A multiplicative factor of 3 for vertical extension of the field lines is used for a better viewing of the configuration.

reconnection is a good mechanism for restructuring the field lines so that the dense material stays below in small reconnected field lines, whereas the large reconnected field lines, released from their weight, get detached from the photosphere and become free to expand. In the case of serpentine field lines, where several BPs are well matched with EBs, we conjecture that local reconnections occur more or less sequentially all along the flux tube, at every BP, so that the serpentine field lines gradually become a standard $\Omega$-loop.

In conclusion, our results on the shape of serpentine lines and on their association with chromospheric brightenings is strong evidence in favor of a multistep flux emergence and $\Omega$-loop formation process: once the subphotospheric large-scale flux tubes becomes flattened and stop their large-scale emergence, small-scale undulations develop and emerge because of the Parker instability. Then magnetic reconnection proceeds at low altitudes in BP separatrices, allowing the release of the dense material that prevents the emergence of the whole flux tube, so that all the small-scale emerged flux tubes sequentially rejoin above the photosphere, forming a large-scale loop, which then becomes free to expand in the corona in the form of AFSs, which then turn into standard coronal loops.

## 6. SUMMARY

During the whole emergence of an active region, the balloon-borne Flare Genesis Experiment (FGE) observed in the H$\alpha$ blue wing the occurrence of many small-scale, intermittent brightenings, defined as Ellerman bombs (EBs), which have been observationally studied by detail in GRBS02 and Bernasconi et al. (2002). In particular, they have shown, using FGE vector magnetograms, that some EBs are cospatial with neutral lines where the field lines could present a U-loop shape (which we defined in this paper as bald patch [BP] regions). So they proposed that some EBs could be due to magnetic reconnection where field lines present a U-loop shape, while the other ones, which were not associated with neutral lines, were probably due to reconnection along quasi-separatrix layers in apparently monopolar regions.

In this paper, we pursued the analysis of EBs observed by FGE, and we tried to tackle the issue of the possible role of these EBs in allowing the emergence of magnetic fields through the
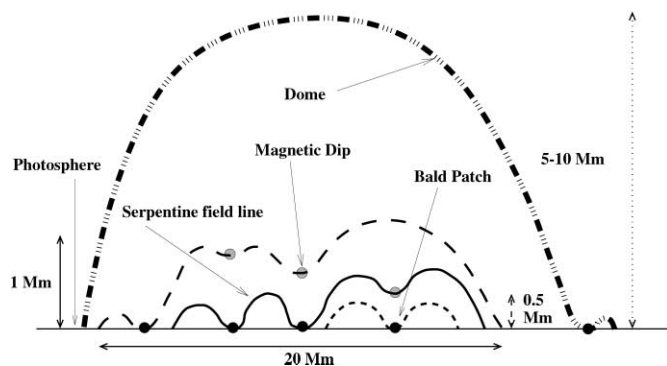


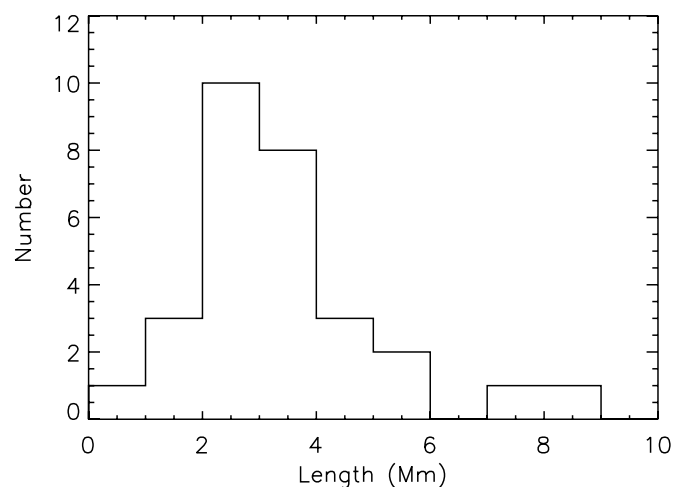Fig. 9.—Sketch of the field lines overlying the emerging flux.



Fig. 10.—Histogram of the distribution of the distance between two consecutive BPs within serpentine field lines.

photosphere. Indeed, MHD simulations have recently shown that the direct emergence of smooth $\Omega$-loops from the convection zone seemed to be more difficult than thought (see, e.g., Zwaan 1985), as a result of both the development of small-scale spatial undulations in subphotospheric flattened flux tubes (stable to the Parker instability; see Magara 2001) and the existence of magnetic dips at the bottom of emerging twisted flux tubes (in which dense material is trapped; see Magara & Longcope 2001 and Fan 2001).

We focused our analysis on one vector magnetogram, observed by FGE nearly cotemporally with one of the H$\alpha$ images showing EBs. From the vector magnetogram, we calculated the three components of the magnetic field in local heliographic coordinates. This permitted us to calculate BP locations from the observations. From this, we not only confirmed the results of GRBS02 and Bernasconi et al. (2002) regarding the good match between EBs and BPs, but we also extended them, since we showed that the apparently monopolar regions in which a few EBs were observed were in fact multipolar and also corresponded to BPs when the magnetic field components were projected onto the heliographic frame. So we unified the two reconnection scenarios proposed by GRBS02 into a single one based on magnetic reconnection along BP separatrices. Nevertheless, there are still a few EBs that cannot be directly explained by the BP scenario and for which the quasi-separatrix layer scenario may be relevant.

In order to calculate the magnetic separatrices, we then performed a linear force-free field extrapolation of the magnetogram, using the true vertical field as the boundary condition. The force-free parameter $\alpha$ was fine-tuned so as to obtain a good match between the observed and extrapolated horizontal components of the magnetic field. We checked a posteriori that the extrapolated high-altitude field lines did not deviate too much from the overall orientation of coronal loops observed in EUV by *TRACE*. Using the results from the extrapolation, we analyzed the three-dimensional topology of the magnetic field at low altitude in the vicinity of EBs. We noticed some subtle differences in the EB-BP correlation, whether calculated from the vector magnetic field data only or from the extrapolation, in which the horizontal fields are calculated so as to satisfy the force-free field equation. With the extrapolation in particular, we found a nonnegligible fraction of EBs that were colocated with the footpoint of a BP separatrix, instead of always being located on top of a BP. These results extended the reconnection scenario for EBs, by locating their brightening either in BPs or at the footpoints of flat BP separatrices, in regions where the magnetic field is horizontal. This result is in fact fully consistent with radiation model predictions by Zhao et al. (1998) and Hénoux et al. (1998).

A further study of the BP separatrices has revealed that the latter were not randomly organized. In several places within the active region, we found some flat, elongated flux tubes linking several BPs (or very low altitude photospheric magnetic dips) and showing spatial undulations with a succession of two to five concave and convex portions. This finding is consistent with the predictions by Strous et al. (1996) on the existence of

magnetic serpentine field lines based on the observation of H$\alpha$ upflows and downflows located one after the other on top of complex multipolar photospheric magnetic fields. Moreover, we identified a whole hierarchy of serpentine field lines, located on top of one another up to chromospheric altitudes, having very small BP separatrices under them and being overlaid with a "dome flux tube" rooted in a single BP region near one of the active region sunspots. This hierarchy of serpentine field lines also seems to be consistent with the results of Mandrini et al. (2002) on the topology of emerging arch filament systems (AFSs), which in the frame of the present study could be interpreted as a dome flux tube under which many serpentine field lines could still be present, even though they did not appear in this past study, maybe because of the poor resolution of their magnetogram, as compared to those from the FGE.

Based on the results of the extrapolation, on the association of EBs with BP and separatrix footpoints, and on the existence and organization of serpentine flux tubes whose wavelengths are typically above (with a sharp cutoff) the criterion for the Parker instability ($\lambda \sim 2$ Mm), we finally conjectured that EBs could be the manifestation of the successive resistive emergence of flattened and undulatory subphotospheric, Parker-unstable flux tubes, which without resistive effects would not fully emerge because of the weight of the material trapped within the (sub)photospheric dips. This interpretation is somehow consistent with the scenario proposed by Strous & Zwaan (1999), but it highlights the crucial role of resistive effects in BP separatrices.

Theoretically, this scenario will need to be confirmed by high-resolution MHD simulations, because even though our observations and extrapolation seem to support BP reconnection for EBs (which also has been shown for a few small flares and surges, e.g., by Aulanier et al. 1998 and Mandrini et al. 2002), the possibility of developing sufficiently thin electric current sheets within flux tubes that have a photospheric dip, so that not only diffusion but impulsive reconnection can occur, is still a debated issue (Low & Wolfson 1988; Karpen et al. 1991; Billinghurst et al. 1993). Our whole analysis, which is as yet only based on a single emerging active region, will have to be reconducted observationally on several regions, for which higher spatial resolution vector magnetograms with high polarimetric sensitivity will be mandatory. This will be required to measure the statistical relevance of our model for the resistive emergence of Parker-unstable undulatory flux tubes in the early stages of active regions.

REFERENCES

Alissandrakis, C. E. 1981, A&A, 100, 197
Aulanier, G., Démoulin, P., Schmieder, B., Fang, C., & Tang, Y. H. 1998, Sol. Phys., 183, 369
Bernasconi, P. N., Rust, D. M., & Eaton, H. A. C. 2001, in ASP Conf. Ser. 236, Advanced Solar Polarimetry—Theory, Observation, and Instrumentation, ed. M. Sigwarth (San Francisco: ASP), 399
Bernasconi, P. N., Rust, D. M., Eaton, H. A. C., & Murphy, G. A. 2000, Proc. SPIE, 4014, 214
Bernasconi, P. N., Rust, D. M., Georgoulis, M. K., & Labonte, B. J. 2002, Sol. Phys., 209, 119
Billinghurst, M. N., Craig, I. J. D., & Sneyd, A. D. 1993, A&A, 279, 589
Caligari, P., Moreno-Insertis, F., & Schüssler, M. 1995, ApJ, 441, 886

Chen, P.-F., Fang, C., & Ding, M.-D. 2001, Chinese J. Astron. Astrophys., 1, 176

Delannée, C., & Aulanier, G. 1999, Sol. Phys., 190, 107

Démoulin, P., Bagalá, L. G., Mandrini, C. H., Hénoux, J. C., & Rovira, M. G. 1997, A&A, 325, 305

Démoulin, P., & Priest, E. R. 1997, Sol. Phys., 175, 123

Ellerman, F. 1917, ApJ, 46, 298

Emonet, T., & Moreno-Insertis, F. 1998, ApJ, 492, 804

Fan, Y. 2001, ApJ, 554, L111

Fletcher, L., López Fuentes, M. C., Mandrini, C. H., Schmieder, B., Démoulin, P., Mason, H. E., Young, P. R., & Nitta N. 2001, Sol. Phys., 203, 255

Gary, G. A., & Hagyard, M. J. 1990, Sol. Phys., 126, 21

Georgoulis, M. K., Rust, D. M., Bernasconi, P. N., & Schmieder, B. 2002, ApJ, 575, 506 (GRBS02)

Handy, B. N., et al. 1999, Sol. Phys., 187, 229

Hénoux, J.-C., Fang, C., & Ding, M. D. 1998, A&A, 337, 294

Karpen, J. T., Antiochos, S. K., & DeVore, C. R. 1991, ApJ, 382, 327

Kitai, R., & Muller, R. 1984, Sol. Phys., 90, 303

Kurokawa, H., Kawaguchi, I., Funakoshi, Y., & Nakai, Y. 1982, Sol. Phys., 79, 77

Leka, K. D., & Skumanich, A. 1999, Sol. Phys., 188, 3

Li, X. Q., Song, M. T., Hu, F. M., & Fang, C. 1997, A&A, 320, 300

Litvinenko, Yu. E., & Somov, B. V. 1994, Sol. Phys., 151, 265

Low, B. C., & Wolfson, R. 1988, ApJ, 324, 574

Magara, T. 2001, ApJ, 549, 608

Magara, T., & Longcope, D. W. 2001, ApJ, 559, L55

Malherbe, J. M., Schmieder, B., Mein, P., Mein, N., van Driel-Gesztelyi, L., & von Uexküll, M. 1998, Sol. Phys., 180, 265

Mandrini, C. H., Démoulin, P., Schmieder, B., Deng, Y. Y., & Rudawy, P. 2002, A&A, 391, 317

Metcalf, T. R., Jiao, L., McClymont, A. N., Canfield, R. C., & Uitenbroek, H. 1995, ApJ, 439, 474

Mickey, D. L., Canfield, R. C., Labonte, B. J., Leka, K. D., Waterson, M. F., & Weber, H. M. 1996, Sol. Phys., 168, 229

Parker, E. N. 1966, ApJ, 145, 811

Priest, E. R., & Démoulin, P. 1995, J. Geophys. Res. A, 100, 23443

Qiu, J., Ding, M. D., Wang, H., Denker, C., & Goode, P. R. 2000, ApJ, 544, L157

Régnier, S., Amari, T., & Kersalé, E. 2002, A&A, 392, 1119

Rust, D. M. 1968, in IAU Symp. 35, Structure and Development of Solar Active Regions, ed. K. O. Kiepenheuer (Dordrecht: Reidel), 77

Scherrer, P. H., et al. 1995, Sol. Phys., 162, 129

Schmieder, B., Aulanier, G., Démoulin, P., van Driel-Gesztelyi, L., Roudier, T., Nitta, N., & Cauzzi, G. 1997, A&A, 325, 1213

Schmieder, B., Démoulin, P., Aulanier, G., & Golub, L. 1996, ApJ, 467, 881

Schmieder, B., Rust, D. M., Georgoulis, M. K., Démoulin, P., & Bernasconi, P. N. 2004, ApJ, 601, 530

Spruit, H. C. 1981, A&A, 98, 155

Strous, L. H. 1994, in Solar Surface Magnetism, ed. R. J. Rutten & C. J. Schrijver (NATO ASI Ser. C, 433; Dordrecht: Kluwer), 73

Strous, L. H., Scharmer, G., Tarbell, T. D., Title, A. M., & Zwaan, C. 1996, A&A, 306, 947

Strous, L. H., & Zwaan, C. 1999, ApJ, 527, 435

Titov, V. S., Priest, E. R., & Démoulin, P. 1993, A&A, 276, 564

Tsuneta, S., et al. 1991, Sol. Phys., 136, 37

Vorpahl, J., & Pope, T. 1972, Sol. Phys., 25, 347

Wang, T., Yan, Y., Wang, J., Kurokawa, H., & Shibata, K. 2002, ApJ, 572, 580

Zhao, X., Fang, C., & Hénoux, J.-C. 1998, A&A, 330, 351

Zwaan, C. 1985, Sol. Phys., 100, 397